Development of a behavior maps tool to evaluate drive operational boundaries and optimization assessment of PMa-SynRMs

C. López-Torres, *Member, IEEE,* C. Colls, A. Garcia, *Member, IEEE,* J. Riba, *Member, IEEE* and L. Romeral, *Member, IEEE*

***Abstract*— The trend in traction motor design and optimization is to achieve high torque and power densities, wider speed range and high efficiency within the area defining the most frequent operating points. A fast tool to evaluate different variables within the torque-speed map is convenient for this purpose. In this context, starting from a preliminary motor design, and taking into account motor cross-coupling effects and power losses, this paper presents a new tool for evaluating the behavior of permanent magnet machines, such as synchronous reluctance machines, and permanent magnet assisted synchronous reluctance machines, in all operational points. Apart from the torque and efficiency, many other electrical variables can be obtained, such as the current space vector angle, power factor or electrical power among others. The proposed tool also allows optimizing the design of the machine under a pre-established control law, thus obtaining the current set point trajectory in the *dq* frame and allowing a fast and accuarate evaluation of motor performance. The results obtained by means of the proposed simulation tool are compared against finite element analysis simulations and experimental data, thus validating the usefulness and accuracy of the proposed methodology.**

***Index Terms*— Design, Electric Motors, Electromagnetic analysis, optimization**

NOMENCLATURE

B	Magnetic flux density [T]
$\hat{B}_{\text{yoke}}$	Peak of Magnetic flux density of yoke [T]
$\hat{B}_{\text{teeth}}$	Peak of Magnetic flux density of teeth [T]
H_c	Coercive force [A/m]
f_s	Electric frequency [Hz]
I_f	Phase current [A]
i_{max}	Maximum current vector amplitude (peak value)[A]
i_{cd}	*d*-axis core loss current [A]
i_d	*d*-axis stator current [A]
i_{od}	*d*-axis torque-generating current [A]
i_{cq}	*q*-axis core loss current [A]
i_q	*q*-axis stator current [A]
i_{oq}	*q*-axis torque-generating current [A]
l	Length of the magnetic reluctance [m]
L_d	*d*-axis magnetizing inductance [H]
L_q	*q*-axis magnetizing inductance [H]
k_e	Eddy current losses coefficient
k_{fe}	Empirical correction coefficient
k_h	Hysteresis losses coefficient
m	Phase number
m_{yoke}	Total mass of yoke [kg]
m_{teeth}	Total mass of teeth [kg]
MMF_i	Magneto-motive force in teeth
MMF_{PM}	Magneto-motive force in magnets
n_i	Exponent hysteresis losses coefficient
N	Number of conductors on each slot
p	Pole pairs
P_{cu}	Copper losses [W]
P_{fe}	Iron losses [W]
P_h	Hysteresis losses [W]
P_i	Heat flow rate between nodes i-th [W]
$P_{ij,ih}$	Losses in node *i*-th [W]
P_e	Eddy current losses [W]
R_{fe}	Iron resistance [Ω]
$R_{ij,ih}$	Thermal resistance between nodes [º/W]
R_s	Phase resistance [Ω]
S	Cross-section of the magnetic reluctance [m^2]
u_{max}	Maximum voltage vector amplitude (peak value)[V]
u_{cd}	*d*-axis core voltage [V]
u_d	*d*-axis stator voltage [V]
u_{cq}	q-axis core voltage [V]
u_q	*q*-axis stator voltage [V]
T	Torque [Nm]
W_q	Magnet width [m]
ε_α	Error of current angle calculation
ε_B	Error of magnetic flux density calculation
ε_{Rfe}	Error of iron resistance calculation
ω_e	Electrical angular speed [rad/s]
ψ_{pmd}	*d*-axis permanent magnet flux linkage [Wb]
ψ_{pmq}	*q*-axis Permanent Magnet flux linkage [Wb]
μ	Magnetic permeability [H/m]
ϕ_i	Magnetic flux on each reluctance [Wb]
θ_i	Temperature in node *i*-th [ºC]
ϕ_d	*d*-position magnetic flux linkage [Wb]
ϕ_q	*q*-position magnetic flux linkage [Wb]
$\Re_{ij}$	Reluctance [H^{-1}]

I. INTRODUCTION

ELECTRICAL machines intended for critical applications, such as electric vehicles (EV), hybrid electric vehicles (HEV) or aeronautics, among others, are increasingly demanding improved performance in terms of power density, wider constant power range and efficiency over specific torque

This work is submitted to review on October 25th, 2017. This work was supported in part by the Spanish Ministry of Economy and Competitiveness under the TRA2013-46757-R Research Project.

C. López, A. Garcia and J. Riba are with the Electrical Engineering Department, Universitat Politècnica de Catalunya (UPC), Spain (carlos.lopez@mcia.upc.edu, garciae@ee.upc.edu and riba@ee.upc.edu).

L. Romeral and C. Colls is with the Electronic Engineering Department, Universitat Politècnica de Catalunya (UPC), Spain (luis.romeral@mcia.upc.edu).

and speed ranges of operation [1, 2]. Permanent magnet synchronous machines (PMSMs) in all their variants [3-5] have received much attention in the last years due to their high efficiency and torque density [6]. Those appealing features are founded in the use of powerful rare-earth magnets, usually made of neodymium (Nd) and a minor content of dysprosium (Dy), whose cost can account for more than 65% of the total materials bill [7]. For that reason, manufacturers have focused their attention in other topologies such as PMa-SynRM (permanent magnet assisted synchronous reluctance machine) or SynRM with the aim to reduce the use of the rare-earth materials, by replacing the PM by hard ferrites, or removing them completely. From these topologies, the concept of rare-earth less or rare-earth free machines [8, 9] arises. Design and optimization of these motor topologies have received much interest in the past years. Traditionally, initial design stages are thought in terms of constraints in different domains, which can include the magnetic, thermal, electrical, mechanical or acoustic domains. The design process tries to reduce the interaction of these different domains to keep the design process as linear as possible. Since electromagnetic and thermal domains are strongly linked, they are often solved together, and afterwards, the other domains are evaluated [10]. Behavior maps, which are a multi-dimensional representation of datasets including different motor variables, are well suited for design assessment in motors [11], since they allow calculating the energy consumption of a specific driving cycle [12, 13]. Efficiency maps are commonly obtained through finite elements analysis (FEA) or experimental analysis [14], whereas power losses are evaluated following specific control strategies such as the MTPA (maximum torque per ampere), MTPV (maximum torque per voltage) [15], or ME (maximum efficiency) trajectories [16]. However, an accurate computation of all possible operating points by means of FEA is very computationally intensive.

This work presents a tool based on behavior maps, which is intended for evaluating drive operational boundaries and optimization assessments of PMa-SynRMs, which avoids an intensive use of FEA. Behavior maps are capable of analyzing motor operation conditions and design characteristics. They are also useful for optimization and control purposes [17], since they can analyze a broad range of operating points, instead of analyzing the rated value or a single point, as done in traditional approaches[18]. By computing hundreds or thousands of operating points in a few seconds by using a detailed *dq*-model, this technique is able to provide not only the so-called efficiency map, but also other information such as the power factor, torque angle or minimum losses maps. In addition, MTPA or MTPV, maximum efficiency, constant stator flux linkage, and constant power loss trajectories in the *dq* current axis can be extracted to generate LUTs (lookup tables) for control purposes [19]. This approach generates useful data to generate torque-speed and other behavior maps, such as i_d-i_q planes among others, which can be used for other applications.

The obtained behavior maps are calculated considering non-linear effects such as cross-coupling, saturation and power losses. This paper deals with the concept of range optimization, which is a trending topic focused on the analysis of a large number of operating points, such as those defining the driving cycle [2, 3, 20], instead of the classical design based on a few number of points representing the rated conditions [21]. Although FEA is widely recognized as an effective design tool for electrical machines [2, 3, 20, 22, 23], when applying a range design process based on the evaluation of multiple operating points, the computational burden imposed by such approach severely limits its application [24, 25]. Therefore, accurate mathematical machine models with low computational requirements, which avoid the use of FEA simulations, are appealing. This paper contributes in this area, since the proposed tool, which is based on a detailed and accurate *dq* model of the machine, whose parameters are obtained from a magnetic network, can be used in a range-based design approach or forcontrol applications based on look-up tables, since cross-coupling, saturation and power losses are considered.

II. Motor Parameters Calculation

This section develops models of the analyzed machines to reduce computational requirements, while preserving results accuracy.

A. Magnetic model

In this section, the magnetic network is detailed. The magnetic model, which allows calculating the *dq* inductances $L_d(i_d,i_q)$ and $L_q(i_d,i_q)$, considers cross-coupling saturation effects. It is based on a single reluctance network, which differs from other approaches [26], in which the reluctance network represents the motor behavior without decoupling the *dq*-axes. Therefore, it allows calculating the interaction between these two magnetic axes. Fig. 1 displays one magnetic pole of the machine.

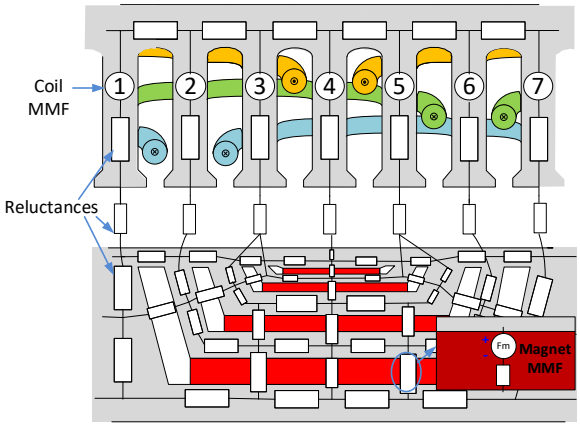

Fig. 1. Reluctance network of the PMa-SynRM proposed in this work. The magnets are highlighted in red color.

The magneto-motive force (MMF) due to the coils (1), which are located on teeth, the reluctances (2) and the MMF of the permanent magnets (3) are calculated, respectively, as,

$$MMF_{1,2...7} = \sum_{1}^{3} NI_f \tag{1}$$

Where sub index on MMF represents the number of teeth.

$$\Re = \frac{l}{\mu(B)\cdot S} \tag{2}$$

$$MMF_{PM} = H_c W_{qi} \tag{3}$$

In order to consider saturation effects, the unknown values ϕ and $\mu(B)$ are obtained from (4) and (5) by applying an iterative approach.

$$\begin{bmatrix} MMF_1 \\ \vdots \\ MMF_n \end{bmatrix} = \begin{bmatrix} \Re_{11} & \cdots & \Re_{1n} \\ \vdots & \ddots & \vdots \\ \Re_{n1} & \cdots & \Re_{nn} \end{bmatrix} \cdot \begin{bmatrix} \phi_1 \\ \vdots \\ \phi_n \end{bmatrix} \tag{4}$$

$$\sum \phi = 0 \tag{5}$$

The *dq* inductances, which take into account cross-coupling effects, are calculated from (6) and (7), and are solved for all considered voltage and current angles.

$$L_d = (\phi_d(i_d, i_q) - \psi_{pmd}) / i_d \tag{6}$$

$$L_q = (\phi_q(i_d, i_q) - \psi_{pmq}) / i_q \tag{7}$$

In order to calculate the inductance (6-7) considering the cross-coupling saturation, the equation system formed by (4-6) must be solved for all *dq*-current combination. Note that the reluctance depends on the solution, so an iterative approach is required. Algorithm 1 shows the proposed procedure to obtain the *dq*-inductances.

1: Set limits to *dq*-current
2: **for** $i_d = 0$ to $i_d = i_{dmax}$ **do**
3: **for** $i_q = 0$ to $i_q = i_{qmax}$ **do**
4: use Park transformation from *dq* to *abc* currents
5: calculate the MMF on each tooth (1)
6: calculate the reluctance (2) using a seed value for *B*
7: **while** average $\varepsilon_B >$ threshold
8: solve the equation system (4-5)
9: Calculate the average error $\varepsilon_B = \left|\frac{B - B_{estimated}}{B}\right|$
10: Calculate the reluctances (2) with the new B
11: **end**
12: use Park transformation from *abc* to *dq* magnetic flux
13: calculate the *dq*-inductances (6,7)
14: **end**
15: **end**

Algorithm 1. Solving procedure to obtain the inductance current dependency

When $i_q = 0$, ϕ_q is the flux linkage ψ_{pmq} of the magnet in the *q*-axis, whereas when $i_d = 0$, ϕ_d is the flux linkage ψ_{pmd} of the magnet in the *d*-axis. Therefore, the model allows calculating the magnet flux linkage depending on the current.

B. Thermal model

The thermal model is based on a thermal network, where the motor geometry is represented as a thermal resistance [27]. Fig. 2 shows a node of the thermal network applied to evaluate the thermal behavior of the machine.

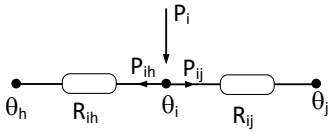

Fig. 2. Thermal node

According to Fig. 2, the thermal equation in the *i*-th node can be written as,

$$P_i = P_{ij} + P_{ih} = \frac{\theta_j - \theta_i}{R_{ij}} + \frac{\theta_h - \theta_i}{R_{ih}} \tag{8}$$

P_i represents the losses associates to the node *i*-th, for instance the iron or copper losses, meanwhile P_{ij} and R_{ij} are the heat flow rate and the thermal resistance between nodes *i* and *j*, respectively. The following thermal equations system is obtained by evaluating all nodes of the thermal network,

$$\begin{bmatrix} \theta_1 \\ \vdots \\ \theta_n \end{bmatrix} = \begin{bmatrix} G_{11} & \cdots & G_{1n} \\ \vdots & \ddots & \vdots \\ G_{n1} & \cdots & G_{nn} \end{bmatrix}^{-1} \begin{bmatrix} P_1 \\ \vdots \\ P_n \end{bmatrix} \tag{9}$$

$G_{ij} = 1/R_{ij}$ being the thermal conductance between nodes *i* and *j*. The temperature θ_i in any node of the thermal network can be calculated for all current and speed values by applying an iterative process, thus allowing to calculate the change of the phase resistance of all elements of the thermal network.

The thermal model is important because some parameters are affected by the temperature. For example, the value the phase resistance and the magnetic properties of the magnets are affected by the temperature.

C. Electric model

The steady-state equations that define the machine behavior in the *dq* rotor reference frame are as follows,

$$u_d = R_S i_d - \omega_e L_q i_{oq} - \omega_e \psi_{pmq} \tag{10}$$

$$u_q = R_S i_q + \omega_e L_d i_{od} + \omega_e \psi_{pmd} \tag{11}$$

$$T = \frac{3}{2} p \left(\psi_{pmd} i_{oq} - \psi_{pmq} i_{od} + \left(L_d - L_q\right) i_{oq} i_{od} \right) \tag{12}$$

The direct axis *d* is tied to the positive axis of the flux vector. Depending on the permanent magnet flux component and inductances ratio, different machine models can be obtained from (8)-(10).

Fig. 3 displays the general equivalent circuit of the abovementioned electrical machines. The term R_{fe} accounts for the iron losses, which includes eddy current and hysteresis losses [28]. It is noted that leakage inductances have been disregarded.

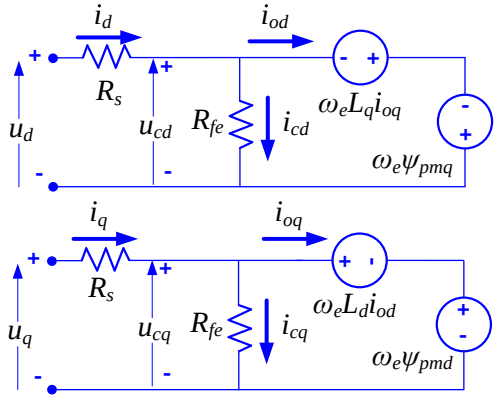

Fig. 3. *d* and *q* axes steady state model in the rotor flux reference frame for different machine topologies.

Based on the circuit shown in Fig. 3, the following equations are deduced,

$$i_d = i_{od} + i_{cd} \tag{13}$$

$$i_q = i_{oq} + i_{cq} \tag{14}$$

$$i_{cd} = \frac{-\omega_e L_q i_{oq} - \omega_e \psi_{pmq}}{R_{fe}} \tag{15}$$

$$i_{cq} = \frac{\omega_e L_d i_{od} + \omega_e \psi_{pmd}}{R_{fe}} \tag{16}$$

From (13)-(16), and by applying Kirchoff's laws, the following equations emerge,

$$i_{od} = \frac{i_d + \frac{\omega_e L_q i_q}{R_{fe}} + \frac{\omega_e \psi_{pmq}}{R_{fe}} - \frac{\omega_e^2 L_q \psi_{pmd}}{R_{fe}^2}}{1 + \frac{\omega_e^2 L_q L_d}{R_{fe}^2}} \tag{17}$$

$$i_{oq} = i_q - \frac{\omega_e \psi_{pmd}}{R_{fe}} - \frac{i_d \omega_e L_d}{R_{fe}\left(1 + \frac{\omega_e^2 L_q L_d}{R_{fe}^2}\right)} - \frac{\omega_e^2 \left(L_d L_q i_q + L_d \psi_{pmq}\right)}{R_{fe}^2 \left(1 + \frac{\omega_e^2 L_q L_d}{R_{fe}^2}\right)} + \frac{\omega_e^3 L_d L_q \psi_{pmd}}{R_{fe}^3 \left(1 + \frac{\omega_e^2 L_q L_d}{R_{fe}^2}\right)} \tag{18}$$

D. Losses model

Copper losses are evaluated by neglecting both skin and proximity effects. The phase resistance can be updated according to the operating temperature if the dependence function is known, or a thermal model is coupled with the electrical model.

$$P_{Cu} = m R_s \frac{i_{\max}^2}{2} [W] \tag{19}$$

The iron losses model the hysteresis and eddy current losses components. Hysteresis losses take into account the *B-H* magnetization curve, whereas eddy current losses include the currents induced by the electromotive force generated in the stator core.

$$P_h = (k_h f_s \hat{B}_{teeth}^{n_i} m_{teeth}) + (k_h f_s \hat{B}_{yoke}^{n_i} m_{yoke}) [W] \tag{20}$$

$$P_e = (k_e f_s^2 \hat{B}_{teeth}^2 m_{teeth}) + (k_e f_s^2 \hat{B}_{yoke}^2 m_{yoke}) [W] \tag{21}$$

These losses are evaluated within the stator yoke and teeth, since the iron losses in the rotor can be neglected [29]. The presence of field harmonics and stresses created within the material during the manufacturing process causes the iron losses to be higher than the results calculated in (20-21), so an empirical correction coefficient is introduced [30],

$$P_{fe} = P_h + P_e = k_{fe}\left(k_h f_s \hat{B}^{n_i} + k_e f_s^2 \hat{B}^2\right)\left[\frac{W}{kg}\right] \tag{22}$$

The hysteresis and eddy current coefficients are evaluated for a particular core material by using the specific core loss in W/kg obtained from the manufacturer's datasheet. Once the iron losses are evaluated, the iron resistance can be calculated as,

$$R_{fe} = m\frac{(u_{cd}^2 + u_{cd}^2)}{2P_{fe}} = \frac{m}{2P_{fe}}\left[\left(-\omega_e L_q i_{oq} - \omega_e \psi_{pmq}\right)^2 + \left(\omega_e L_d i_{od} + \omega_e \psi_{pmd}\right)^2\right] \tag{23}$$

E. Drive operation boundaries

The motor behavior is characterized in all possible operating points, which comprise voltage, current and frequency combinations. The limit values for those variables are settled by the converter, although they can be exceeded when analyzing the motor behavior beyond rated conditions, for example to explore its fault tolerant capability. In this context, (10), (11), (13) and (14) must fulfil,

$$u_d^2 + u_q^2 \le u_{\max}^2 \tag{24}$$

$$i_d^2 + i_q^2 \le i_{\max}^2 \tag{25}$$

These equations can be expressed in the *dq* current plane. By replacing (10) and (11) into (24) and replacing the *dq* torque generating currents i_{od} and i_{oq} by (17) and (18), a second order equation is obtained,

$$A i_d^2 + B i_d i_q + C i_q^2 + D i_d + E i_q + F = 0 \tag{26}$$

The geometrical representation of (26) is shown in Fig. 4, whereas the coefficients of (26) are detailed in Table I.

TABLE I
COEFFICIENTS IN EQUATION (28)

$A = k_1^2 + k_5^2$	$D = 2(k_1 k_3 + k_6 k_5)$
$B = 2(k_1 k_2 + k_4 k_5)$	$E = 2(k_3 k_2 + k_4 k_6)$
$C = k_2^2 + k_4^2$	$F = k_3^2 + k_6^2 - u_{\max}^2$

The different coefficients k_i (i = 1, 2…6) shown in Table II depend on motor parameters such as the *dq* inductances, angular speed, phase and iron resistances and *dq* magnet flux linkage.

Table II
DETAILED SECOND GRADE COEFFICIENTS k_i

$k_1 = R_s + \frac{\omega_e^2 L_d L_q}{R_{fe}\left(1 + \frac{\omega_e^2 L_d L_q}{R_{fe}^2}\right)}$	$k_4 = k_1$
$k_2 = -\omega_e L_q + \frac{\omega_e^3 L_d L_q^2}{R_{fe}^2\left(1 + \frac{\omega_e^2 L_d L_q}{R_{fe}^2}\right)}$	$k_5 = \frac{\omega_e L_d}{\left(1 + \frac{\omega_e^2 L_d L_q}{R_{fe}^2}\right)}$
$k_3 = \frac{\omega_e^3 L_d L_q \psi_{pmq}}{R_{fe}^2\left(1 + \frac{\omega_e^2 L_d L_q}{R_{fe}^2}\right)} - \omega_e \Psi_{pmq} + \frac{\omega_e^2 L_q \psi_{pmd}}{R_{fe}} - \frac{\omega_e^4 L_d L_q^2 \psi_{pmd}}{R_{fe}^3\left(1 + \frac{\omega_e^2 L_d L_q}{R_{fe}^2}\right)}$	
$k_6 = \frac{\omega_e^2 L_d \psi_{pmq}}{R_{fe}\left(1 + \frac{\omega_e^2 L_d L_q}{R_{fe}^2}\right)} + \omega_e \Psi_{pmd} - \frac{\omega_e^3 L_d L_q \psi_{pmd}}{R_{fe}^2\left(1 + \frac{\omega_e^2 L_d L_q}{R_{fe}^2}\right)}$	

Note that the proposed equation system works for different motor topologies. Since the coefficients in (26) consider the possibility to include magnets in both axes. To summarize, depending on the permanent magnet flux component and inductances ratio, different machine models can be obtained. Table III shows the different values of these parameters.

Table III
Detail of machine's parameters depending on motor type

Motor type	Saliency	ψ_{pmd}	ψ_{pmq}
SynRM	$L_d > L_q$	$\psi_{pmd} = 0$	$\psi_{pmq} = 0$
PMaSynRM	$L_d > L_q$	$\psi_{pmd} = 0$	$\psi_{pmq} < 0$
IPMSM	$L_d < L_q$	$\psi_{pmd} > 0$	$\psi_{pmq} = 0$
SPMSM	$L_d = L_q$	$\psi_{pmd} > 0$	$\psi_{pmq} = 0$

The level of detail can be chosen, since the iron losses and copper losses can be neglected. The iron losses can be ignored by assuming the iron resistance to be infinite (coefficients shown on Table II), whereas the copper losses can be neglected by assuming the phase resistance to be zero .

III. SOLVING PROCEDURE

This section deals with a *dq* detailed model of the analyzed electrical machines [31], instead of generating a dynamic reluctance network or using a FEA-based model. The proposed

approach can be further generalized to other motor topologies since the parameters in Table II allows including magnets in both axes. Different effects, such as inductance saturation, iron losses or the analysis of current levels beyond the drive limits are considered. Blondel diagrams are used to ensure feasible results (only voltage and current locus intersections in suitable sectors are computed) and a fast solution, as this method minimizes the number of iterations required. Blondel diagrams allow visualizing the interaction of the machine's voltage, current and torque in a single chart [32]. An example is shown in Fig. 4 for two different machines, an internal permanent magnet synchronous machine (IPMSM) and a permanent magnet assisted synchronous reluctance machine (PMa-SynRM).

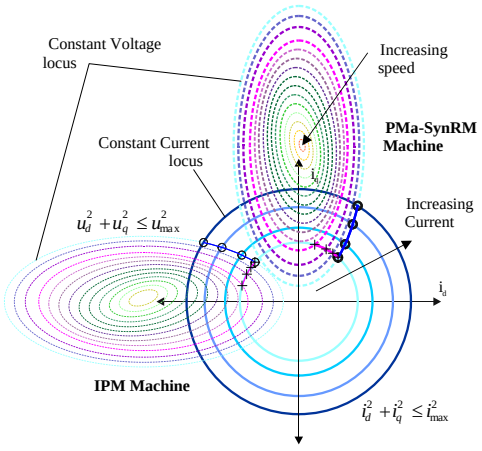

Fig. 4. Solving procedure from the complex *dq* current plane for two machines with their respective voltage locus.

Using the k_i coefficients of Tables III, II and I, it is possible to obtain the position and orientation of the ellipses. Each machine type shown in Table III has its own set of parameters, which determine the values and signs of the coefficients k_i summarized in Table II. The generalized equation of a conic section described in (26) generates different ellipses depending on the values of those coefficients. For example, in Fig. 4, the ellipses describing an IPMSM are oriented along the *d*-axis, while the ones describing a PMa-SynRM are oriented along the *q*-axis. Ellipses rotation and displacement over the speed range are due to the loss coefficients R_{fe} and R_s in Table II. The effect of power loss can be analyzed from (26). For example, when R_{fe} and R_s are neglected, $k_1 = k_4 = 0$, and thus $B = 0$. So, the ellipse axes will be aligned with the axes of the reference frame. Since R_{fe} the R_s are found in all six coefficients k_i, their values will impact the voltage locus, including size, orientation and position. This effect can significantly influence the control laws and torque-speed maps.

To generate the maps characterizing the motor (detailed ensemble of working points), the control parameters are swept within the feasible operating limits. The current is limited by the maximum allowable temperature, the voltage by the insulation requirements and the speed by the mechanical constraints. Those variables (voltage, current and speed) define the three main loops of the code detailed in Fig. 6.

Fig. 5 shows the effect of the sweep applied to a PMa-SynRM. It visualizes both, the current and speed, in the two usual working planes, the *dq* and torque-speed planes. The sweep detail depends on the purpose of the maps. A coarse map (100 rpm, 10 A and 25 V steps) for a 3000 rpm, 50 A, 300 V machine can be useful to study thermal limits. For the same motor, 10 rpm, 1 A and 5 V steps can be more useful for torque angle data acquisition for control purposes. It is important to save, for each working point, all related variables such as voltage, current, speed, torque, resistance, power losses or flux linkage. This allows a further post-processing stage, by selecting the points matching with a target solution, e.g. maximum efficiency or maximum torque.

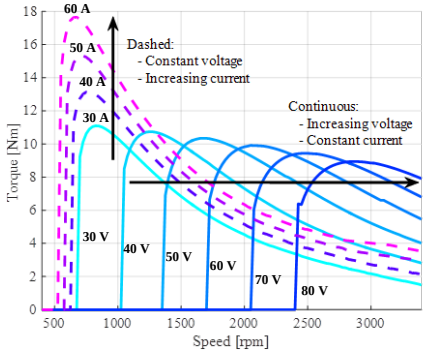

Fig. 5. Solving procedure in the torque-speed plane, showing all voltage-current intersection points for fixed values of voltage or current.

IV. Solving Algorithm

The procedure proposed to solve the different working points of a given machine consists of a succession of embedded loops, which are required to restrict the values of the different variables in (26), which defines the voltage locus. The algorithm applied for this purpose is exposed below.

1: Set the voltage, current and speed steps
2: **for** $u = 0$ to $u = u_{max}$ **do**
3: the term F is obtained (Table I): $F = k_3^2 + k_6^2 - \boldsymbol{u^2}$
4: **for** $i = 0$ to $i = i_{max}$ **do**
5: copper losses and circle calculation
6: **for** $\omega_e = 0$ to $\omega_e = \omega_{max}$ **do**
7: set current angle estimation, $\alpha_{estimated}$
8: **while** $\varepsilon_\alpha >$ threshold **do**
9: from LUT obtain L_d, L_q, ψ_{pmd} and ψ_{pmq}
10: calculate iron losses P_{fe}
11: calculate the iron resistance $R_{fe\,estimated} = \frac{m}{2}\frac{u_{fe}^2}{P_{fe}} \approx \frac{m}{2}\frac{u^2}{P_{fe}}$
12: **while** error of $\varepsilon_{R_{fe}}$ > threshold **do**
13: ellipse determination
14: intersection calculation (i_d,i_q) using (27-28)
15: determination of i_{od} (17), i_{oq} (18), u_d (10), u_q(11), R_{fe}(23), α_i, α_v, T(12) and PF.
16: error calculation $\varepsilon_{R_{fe}} = \left|\frac{R_{fe}-R_{fe\,estimated}}{R_{fe}}\right|$
17: **end**
18: error calculation $\varepsilon_\alpha = \left|\frac{\alpha_i-\alpha_{estimated}}{\alpha_i}\right|$
19: **end**
20: save data
21: **end**
22: **end**
23: **end**

Algorithm 2. Solving procedure to obtain the behaviors maps

For each combination of voltage, current and frequency, the properties of this operational point must be saved. The intersection between current and voltage is done algebraically by applying the following change of variables to decouple the i_d and i_q currents;

$$i_d = i\left(\frac{1-t^2}{1+t^2}\right) \tag{27}$$

$$i_q = i\left(\frac{2t}{1+t^2}\right) \tag{28}$$

where i is the current magnitude considered in each loop and t is the new variable.

The details of Algorithm 2 are shown in Fig. 6, which displays the inputs required and outputs obtained. It includes two subprocesses, the first is the losses calculation step, and the second to obtain the iron resistance.

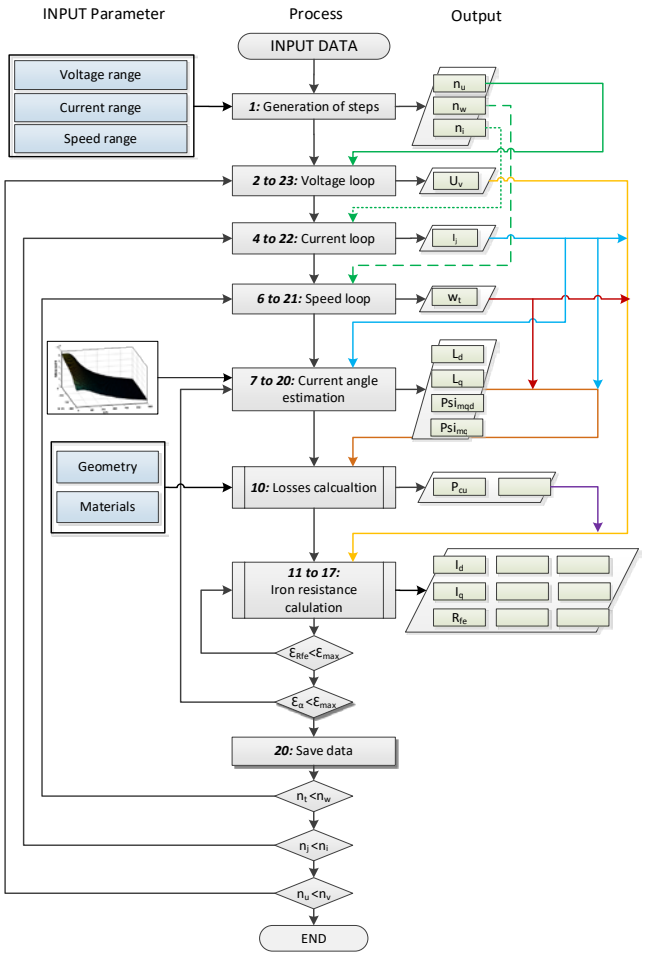

Fig. 6. Flow chart of the process to generate the behavior maps.

The different operating points are calculated by applying this iterative process. It allows parallelization since this approach includes three basic loops (voltage, current and speed), so the related calculations can be split among different cores.

After analyzing all feasible voltage, current and frequency combinations, the machine operating points are acquired. There are many different torque-speed curves (see Fig. 5), which represent different combination of current and voltage. Therefore, the same working point (same torque and speed) can be obtained using different combinations. Next, by manipulating the data included in all operating points, different behavior maps can be obtained.

A mesh grid is created to delimit the number of points in the different behavior maps. In each interval, the different working points are evaluated according to a pre-established control law, and the best one is chosen.

Fig. 7 shows a small area of Fig. 5, which includes the different calculated working points and the properties of each one. In this detail, a torque-speed interval is analyzed to choose the best working point. The selected working point represents the full interval in the behavior map. For instance, when applying the MTPA control law, the chosen operating point would be *d*, since this point has the best torque per ampere ratio in the interval analyzed (30 V, 30 A curve).

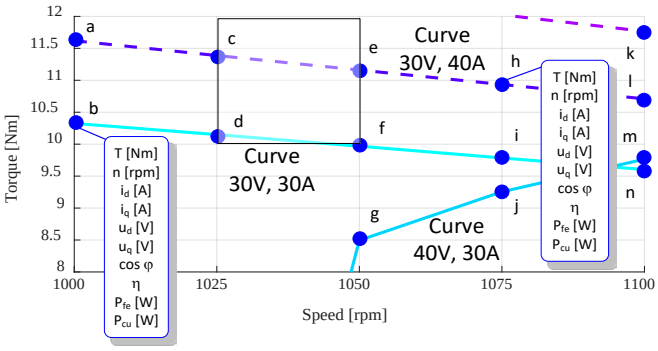

Fig. 7. Detail of the torque-speed points selection depending on designer consideration. All points contain the information listed in *b* or *h*. The square represents a discrete ΔT-Δω 2D-interval.

The size of the mesh grid in the torque speed plane is strongly connected to the number of working points obtained in the process. The higher the resolution desired, the lesser the voltage, current and speed step size required, which affects the number of points in a torque-speed interval.

V. FEA Validation

This section validates the fast tool to assist the optimal design process of electric machines within a given range, against FEA. During the optimization process, a single or multi-objective cost function can be defined in a range of operation, such as maximum torque density, maximum power density or maximum efficiency, among others. More accurate information for motor control purposes can also be obtained, since the MTPA, MLC (minimum losses control) or other control trajectories can be calculated.

The cost function can be evaluated within the considered range, according to the information gathered from each operating point. The proposed fast tool allows calculating essential information for all operating points, including current and voltage components, power factor, output torque, mechanical speed, losses, efficiency, temperature or current angle. All torque-speed planes are evaluated according to the MTPA control law, thus obtaining the different behavior maps for a PMa-SynRM. The main characteristics of the analyzed PMa-SynRM with the methodology proposed are summarized in Table IV.

TABLE IV. MOTOR SPECIFICATIONS

Items [unit]	Value
Mechanical power [kW]	27
Phase voltage [V_{rms}]	104
Phase current [A_{rms}]	170
Corner speed [rpm]	2800
Number of phases	3
Number of poles pairs	8
Number of slots	96
Iron lamination	M300-35A
Ferrite magnet	HF 26/24
Outer stator diameter	270 mm
Stack length	70 mm
Insulation type	H

Fig. 8 shows the efficiency map in the torque-speed plane. It highlights the values of some points for a further comparison with the efficiency map obtained through FEA simulations.

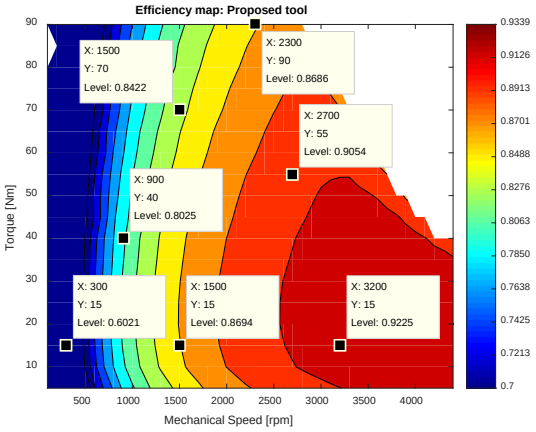

Fig. 8. Efficiency map [p.u.] under the MTPA control law obtained by means of the proposed tool.

The fast calculation of the efficiency map increases the possibility to obtain a better design, considering the most frequent operational torque-speed range. For example, in a traction application, the cost function can be associated to the characteristics of the driving cycle.

An example of the possible behaviors obtained from the torque-speed plane is the power factor, as shown in Fig. 9.

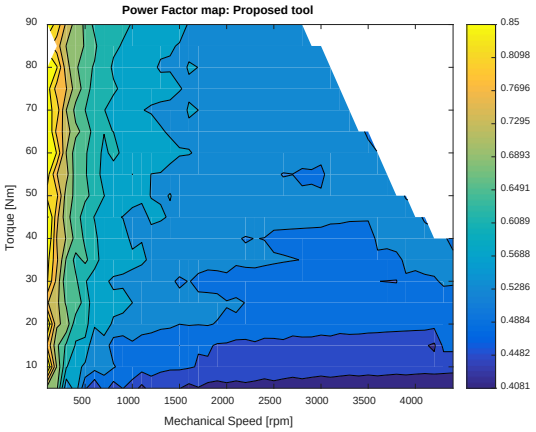

Fig. 9. Power factor [-] map under the MTPA control law obtained by means of the proposed tool.

The power factor in PMa-SynRMs is strongly related to the magnet quantity, so by evaluating the power factor, the magnet usage can be optimized.

As mentioned, other performances can be calculated. Fig. 10 shows the iron losses in the torque-speed plane, whereas Fig. 11 shows the phase voltage for all considered working points. Different magnetic materials can be analyzed to evaluate the iron losses, so the best candidate can be selected by considering both, cost and losses constraints. The voltage torque-speed plane can provide useful information to determine the motor capabilities when dealing with different dc buses, for example to take into account different states of charge of the battery.

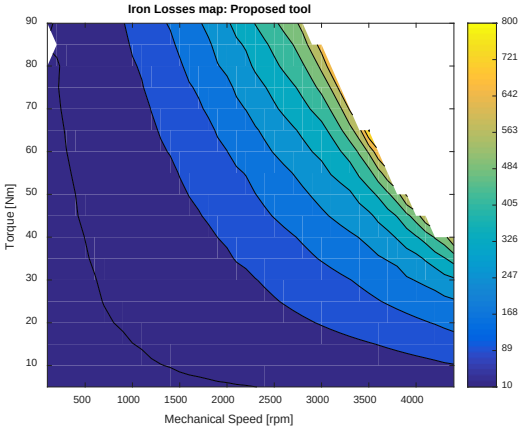

Fig. 10. Iron losses map [W] under the MTPA control law obtained by means of the proposed tool.

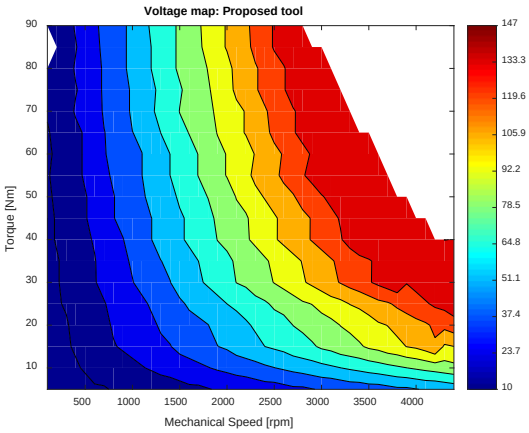

Fig. 11. Phase voltage [V] map under the MTPA control by means of the proposed tool.

It must be pointed out that the control law can be changed at will, for example by applying the MLC or maximum efficiency control laws, with no increase of the computational burden, and the cost function can be re-evaluated in each interval. Therefore, different optimization scenarios considering different control laws can be easily evaluated.

To validate the accuracy of the proposed tool, the motor shown in Table IV has been analyzed using the Flux FEA software (Altair, v12.1). Fig. 12 shows the MTPA efficiency maps generated by means of FEA simulations. A good correspondence between the maps in Figs. 8 and 12 is observed, thus validating the accuracy of the proposed tool since the average error is less than 3%. Note that the marked points have almost the same efficiencies than those in the MTPA efficiency map shown in Fig. 8.

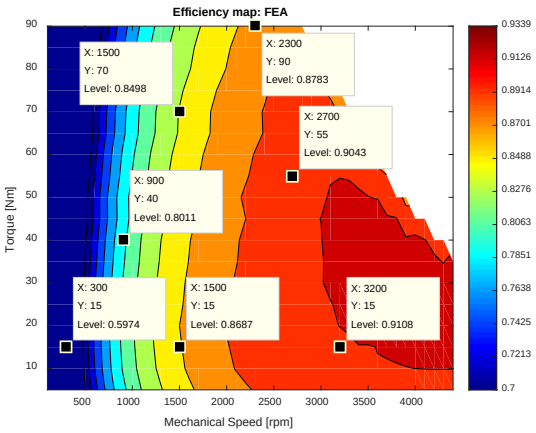

Fig. 12. Efficiency [p.u.] map obtained by means of FEA simulations.

Other behavior maps are calculated to compare FEA results with the ones provided by the proposed tool. For instance, the peak phase voltage is depicted in Fig. 13. The average error in this maps is below 4.5%, being the flux weakening region the zone with more divergence.

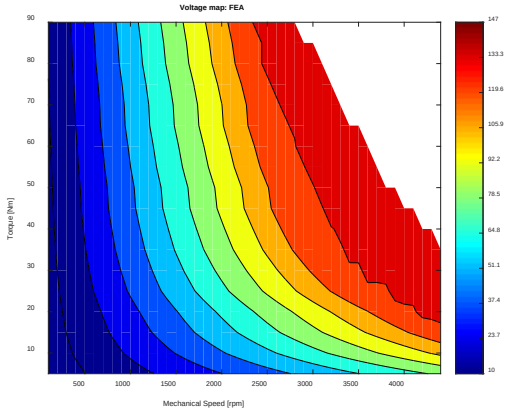

Fig. 13. Phase voltage [V] map obtained by means of FEA simulations

Fig. 14 shows the iron losses map calculated by FEA. It can be observed that the losses in FEA are higher than the obtained by the proposed tool. The average error in this case is 8%. However, in the maximum speed the higher error is 15%. Therefore, the calculation of iron losses (22) can be improved by means of a better discretization of the motor geometry.

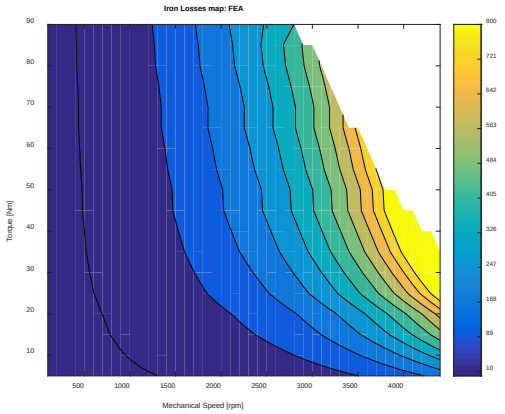

Fig. 14. Iron losses [W] map obtained by means of FEA simulations

Finally, Fig. 15 depicts the power factor in the torque-speed plane. The average error in this case is 6%. The good agreement in the power factor calculation can help in the design process. For example, the size of the converter can be included in the optimization.

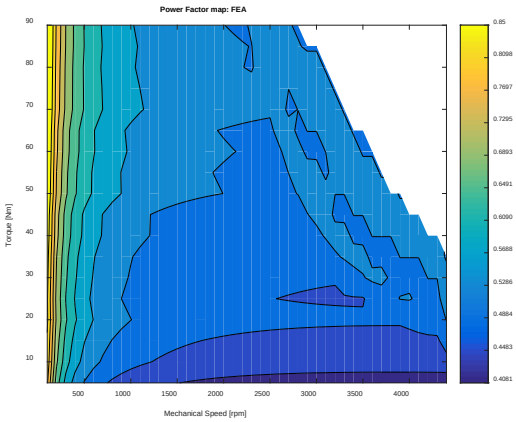

Fig. 15. Power factor [p.u.] obtained by means of FEA simulations

The time required for the proposed tool to process a PMa-SynRM using 70 voltage steps, 120 current steps and 208 speed steps (resulting in a total of 1.747,200 evaluated points) is of about 120 seconds. The data post-processing stage requires about 60 seconds. However, it is worthy to mention that the data necessary to feed the proposed tool has to be calculated. The magnetic and thermal model requires about 100 and 30 seconds, respectively, to obtain the inductances, magnet flux linkage, and the machine temperature. On the other hand, when the FEA software evaluates only 810 points, which correspond to a torque step $\Delta T = 5$ Nm and speed changes of $\Delta n = 100$ rpm, the computational time is of about 6 days. These times are based on a Xeon E5-1620 computer with 32 GB RAM, for both processes.

It is noted that the time required by the proposed fast tool to change any of the variable intervals is only for post-processing, which is of about 60 seconds, since the points are already evaluated. However, the same process with FEA implies to restart the simulations with the new intervals.

VI. Experimental Validation

The validation against FEA, which has been summarized in the previous section, confirms the high accuracy of the proposed methodology. In this section, a further validation is carried out by using experimental data. The experimental validation consists on analyzing several working points and obtaining the current angle that provides the maximum torque per ampere. Then, the results obtained can be compared with the data extracted from the current module and current angle maps obtained by means of the proposed tool. The control allows selecting the current angle manually, in order to sweep the different values to find out the angle with the best torque-ampere ratio.

A representative scheme of the experimental test bench is shown in Fig. 16. A T22 torque sensor from HBM, a RI 76TD encoder from Hengstler, a 1FT6108-8SB71-1DK3 Surface Mounted PMSM from Siemens and a CompactRIO acquisition system were used in the experimental part. A PMA-SynRM

with the characteristics shown in Table IV is examined in this section.

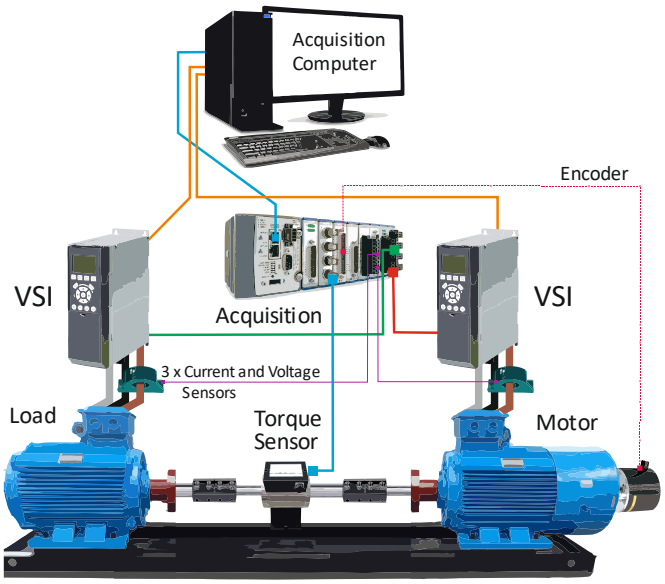

Fig. 16. Representation of the experimental test bench.

As mention before, the results provided by the proposed tool are used to obtain the lookup table for a MTPA control. In order to validate the different behavior maps focused on control purposes, the experimental values of the current angle and phase currents are compared against those obtained by means of the proposed tool. Fig. 17 shows the current angle in the torque-speed plane obtained with the proposed tool. The current angle map is obtained considering the iron losses, phase resistance, and cross-coupling saturation under the maximum torque per ampere law.

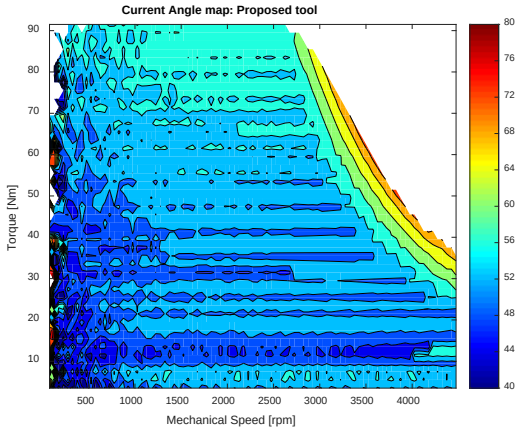

Fig. 17. Current angle [p.u.] obtained by means of the proposed tool under MTPA control law

Then, several combinations of working points are analyzed experimentally. The data obtained are represented in tables to facilitate the comparison with the proposed tool. The tables show the working points (angular speed – torque), values of the estimated parameter, measured parameters, and the percentual error. Table V compares the current space vector angle calculated by means of the proposed fast tool with the experimental one.

TABLE V. CURRENT ANGLE ERROR COMPARISON BETWEEN

Angular speed [rpm]	Torque [Nm]	Estimated current angle [º]	Experimental current angle [º]	Error [%]
300	32	47.9	47.8	0.2
300	60	50.7	51.7	1.9
300	79	55.1	53.8	2.4
700	27	44.8	46.8	4.2
700	57	53.1	51.8	2.5
700	76	55.7	53.9	3.3
1000	35	47.1	48.6	3.0
1000	43	48.9	49.6	1.4
1000	84	55.5	54.7	1.4
1400	47	49.2	50.3	2.1
1400	62	51.4	52	1.1
1400	85	54.6	53.7	2.0
1700	22	45.7	45.9	0.4
1700	76	54.3	53.8	0.9
1700	85	54.8	55.1	0.5
2100	17	45.2	45.1	0.2
2100	55	52.5	51.3	2.3
2100	80	53.5	54.1	1.1
Average	-	-	-	**1.7**

The control parameters require knowing the current angle and the phase current to determine the *dq* currents for all torque-speed combinations. Fig. 18 shows the peak phase current in the torque-speed plane.

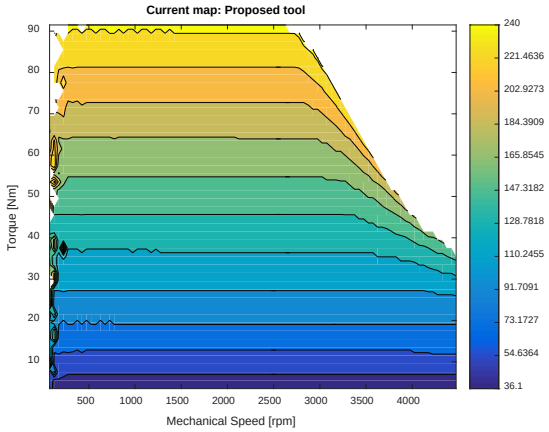

Fig. 18. Phase current [A] obtained by means of the proposed tool under MTPA control law

Table VI compares the phase current calculated by means of the proposed fast tool with the experimental ones.

TABLE VI. PHASE CURRENT ERROR COMPARISON

Angular speed [rpm]	Torque [Nm]	Estimated current [A]	Experimental current [A]	Error [%]
300	32	120	122	1.6
300	60	177	182	2.7
300	79	222	227	2.2
700	27	111	108	2.7
700	57	171	181	5.5
700	76	213	226	5.7
1000	35	126	131	3.8
1000	43	144	148	2.7
1000	85	232	245	2.8
1400	47	153	158	3.1
1400	62	183	190	3.6
1400	85	232	245	5.3
1700	22	99	99	0.0
1700	76	214	226	5.3
1700	85	232	245	5.3
2100	17	87	87	0.0
2100	55	168	175	4.0
2100	80	220	230	4.3
Average	-	-	-	**3.4**

Results summarized in Tables V and VI show a close agreement between the results provided by the proposed simulation tool and the experimental data, thus validating the approach presented in this paper.

VII. Conclusion

This paper has presented a new computationally efficient tool for motor design and optimization purposes. It allows evaluating a broad range of operating conditions and design variables, and dealing with different machine topologies, different magnetic materials and diverse control strategies. The proposed tool greatly speeds up the optimization process of the studied machine. This is an appealing feature, since a FEA-based approach considering all operating points for each possible design result in a tedious and time-consuming process.

The cost function may also deal with range optimization, when required. Multi-objective optimization is typically required for traction applications, where power density, torque ripple, maximum torque or other features are sought. By using the proposed tool, the efficiency, power factor and losses can be considered during the optimization stage within an operational range. For example, the maximum power as well as the efficiency can be increased within the most frequent torque-speed range. Furthermore, the versatility of the tool allows analyzing different motor topologies to choose the best motor configuration for each particular application. FEA and experimental results have validated the accuracy and usefulness of the proposed methodology.

References

[1] S. Ray and D. A. Lowther, "Multi-Objective Optimization Applied to the Matching of a Specified Torque-Speed Curve for an Internal Permanent Magnet Motor," *IEEE Transactions on Magnetics*, vol. 45, no. 3, pp. 1518-1521, 2009.

[2] A. G. Sarigiannidis, M. E. Beniakar, and A. G. Kladas, "Fast Adaptive Evolutionary PM Traction motor Optimization based on Electric Vehicle Drive Cycle," *IEEE Transactions on Vehicular Technology*, vol. PP, no. 99, pp. 1-1, 2016.

[3] K. Ahn, A. E. Bayrak, and P. Y. Papalambros, "Electric Vehicle Design Optimization: Integration of a High-Fidelity Interior-Permanent-Magnet Motor Model," *IEEE Transactions on Vehicular Technology*, vol. 64, no. 9, pp. 3870-3877, 2015.

[4] J. Wang, X. Yuan, and K. Atallah, "Design Optimization of a Surface-Mounted Permanent-Magnet Motor With Concentrated Windings for Electric Vehicle Applications," *IEEE Transactions on Vehicular Technology*, vol. 62, no. 3, pp. 1053-1064, 2013.

[5] X. Liu, H. Chen, J. Zhao, and A. Belahcen, "Research on the Performances and Parameters of Interior PMSM Used for Electric Vehicles," *IEEE Transactions on Industrial Electronics*, vol. 63, no. 6, pp. 3533-3545, 2016.

[6] J. Hochang, K. Deokjin, L. Chun-Beom, A. Jihyun, and J. Sang-Yong, "Numerical and Experimental Design Validation for Adaptive Efficiency Distribution Compatible to Frequent Operating Range of IPMSM," *Magnetics, IEEE Transactions on*, vol. 50, no. 2, pp. 881-884, 2014.

[7] C. Haiwei, G. Bo, and X. Longya, "Low-Cost Ferrite PM-Assisted Synchronous Reluctance Machine for Electric Vehicles," *Industrial Electronics, IEEE Transactions on*, vol. 61, no. 10, pp. 5741-5748, 2014.

[8] J.-R. Riba, C. López-Torres, L. Romeral, and A. Garcia, "Rare-earth-free propulsion motors for electric vehicles: A technology review," *Renewable and Sustainable Energy Reviews*, vol. 57, pp. 367-379, 2016.

[9] M. Kimiabeigi *et al.*, "High-Performance Low-Cost Electric Motor for Electric Vehicles Using Ferrite Magnets," *IEEE Transactions on Industrial Electronics*, vol. 63, no. 1, pp. 113-122, 2016.

[10] A. Fatemi, N. A. O. Demerdash, T. W. Nehl, and D. M. Ionel, "Large-Scale Design Optimization of PM Machines Over a Target Operating Cycle," *IEEE Transactions on Industry Applications*, vol. 52, no. 5, pp. 3772-3782, 2016.

[11] R. Antonello, M. Carraro, A. Costabeber, F. Tinazzi, and M. Zigliotto, "Energy-Efficient Autonomous Solar Water-Pumping System for Permanent-Magnet Synchronous Motors," *IEEE Transactions on Industrial Electronics*, vol. 64, no. 1, pp. 43-51, 2017.

[12] M. Morandin, M. Ferrari, and S. Bolognani, "Power-Train Design and Performance of a Hybrid Motorcycle Prototype," *IEEE Transactions on Industry Applications*, vol. 51, no. 3, pp. 2216-2226, 2015.

[13] K. Emmrich, A. Brune, and B. Ponick, "Evaluation of an analytical, efficiency-optimized torque-speed characteristic of induction machines coupled with a thermal-electromagnetic energy consumption calculation," in *Electrical Machines (ICEM), 2014 International Conference on*, 2014, pp. 762-767.

[14] G. Pellegrino, B. Boazzo, and T. M. Jahns, "Magnetic Model Self-Identification for PM Synchronous Machine Drives," *IEEE Transactions on Industry Applications*, vol. 51, no. 3, pp. 2246-2254, 2015.

[15] B. Cheng and T. R. Tesch, "Torque Feedforward Control Technique for Permanent-Magnet Synchronous Motors," *IEEE Transactions on Industrial Electronics*, vol. 57, no. 3, pp. 969-974, 2010.

[16] S. A. Odhano, R. Bojoi, A. Boglietti, Ş. G. Roşu, and G. Griva, "Maximum Efficiency per Torque Direct Flux Vector Control of Induction Motor Drives," *IEEE Transactions on Industry Applications*, vol. 51, no. 6, pp. 4415-4424, 2015.

[17] D. Q. Dang, M. S. Rafaq, H. H. Choi, and J. W. Jung, "Online Parameter Estimation Technique for Adaptive Control Applications of Interior PM Synchronous Motor Drives," *IEEE Transactions on Industrial Electronics*, vol. 63, no. 3, pp. 1438-1449, 2016.

[18] S. Stipetic, D. Zarko, and M. Kovacic, "Optimised design of permanent magnet assisted synchronous reluctance motor series using combined analytical–finite element analysis based approach," *IET Electric Power Applications*, vol. 10, no. 5, pp. 330-338, 2016.

[19] R. Monajemy and R. Krishnan, "Control and dynamics of constant-power-loss-based operation of permanent-magnet synchronous motor drive system," *IEEE Transactions on Industrial Electronics*, vol. 48, no. 4, pp. 839-844, 2001.

[20] E. Oksuztepe, "In-Wheel Switched Reluctance Motor Design For Electric Vehicles By Using Pareto Based Multi Objective Differential Evolution Algorithm," *IEEE Transactions on Vehicular Technology*, vol. PP, no. 99, pp. 1-1, 2016.

[21] E. Carraro, M. Morandin, and N. Bianchi, "Traction PMASR Motor Optimization According to a Given Driving Cycle," *IEEE Transactions on Industry Applications*, vol. 52, no. 1, pp. 209-216, 2016.

[22] V. Ruuskanen, J. Nerg, J. Pyrhönen, S. Ruotsalainen, and R. Kennel, "Drive Cycle Analysis of a Permanent-Magnet Traction Motor Based on Magnetostatic Finite-Element Analysis," *IEEE Transactions on Vehicular Technology*, vol. 64, no. 3, pp. 1249-1254, 2015.

[23] C. L. Torres, A. Garcia, J. Riba, and L. Romeral, "Design and optimization for vehicle driving cycle of rare-earth-free SynRM based on coupled lumped thermal and magnetic networks," *IEEE Transactions on Vehicular Technology*, vol. PP, no. 99, pp. 1-1, 2017.

[24] S. Taghavi and P. Pillay, "A Novel Grain-Oriented Lamination Rotor Core Assembly for a Synchronous Reluctance Traction Motor With a Reduced Torque Ripple Algorithm," *IEEE Transactions on Industry Applications*, vol. 52, no. 5, pp. 3729-3738, 2016.

[25] M. Ferrari, N. Bianchi, and E. Fornasiero, "Analysis of Rotor Saturation in Synchronous Reluctance and PM-Assisted Reluctance Motors," *IEEE Transactions on Industry Applications*, vol. 51, no. 1, pp. 169-177, 2015.

[26] C. L. Torres, T. Michalski, A. G. Espinosa, and L. Romeral, "Fast optimization of the magnetic model by means of reluctance network for PMa-SynRM," in *IECON 2016 - 42nd Annual Conference of the IEEE Industrial Electronics Society*, 2016, pp. 1642-1647.

[27] C. L. pez, T. Michalski, A. Espinosa, and L. Romeral, "New SynRM design approach based on behaviour maps analysis," in *2016 XXII International Conference on Electrical Machines (ICEM)*, 2016, pp. 1915-1921.

[28] F. Fernandez-Bernal, A. Garcia-Cerrada, and R. Faure, "Determination of parameters in interior permanent-magnet synchronous motors with iron losses without torque measurement," *IEEE Transactions on Industry Applications*, vol. 37, no. 5, pp. 1265-1272, 2001.

[29] K. Yamazaki and H. Ishigami, "Rotor-Shape Optimization of Interior-Permanent-Magnet Motors to Reduce Harmonic Iron Losses," *IEEE Transactions on Industrial Electronics*, vol. 57, no. 1, pp. 61-69, 2010.

[30] N. Zhao and W. Liu, "Loss Calculation and Thermal Analysis of Surface-Mounted PM Motor and Interior PM Motor," *IEEE Transactions on Magnetics*, vol. 51, no. 11, pp. 1-4, 2015.

[31] D. G. Dorrell, M. Hsieh, M. Popescu, L. Evans, D. A. Staton, and V. Grout, "A Review of the Design Issues and Techniques for Radial-Flux Brushless

Surface and Internal Rare-Earth Permanent-Magnet Motors," *Industrial Electronics, IEEE Transactions on*, vol. 58, no. 9, pp. 3741-3757, 2011.

[32] R. H. Moncada, J. A. Tapia, and T. M. Jahns, "Saliency analysis of PM machines with flux weakening capability," in *Electrical Machines, 2008. ICEM 2008. 18th International Conference on*, 2008, pp. 1-6.